Communications on Applied Nonlinear Analysis
ISSN: 1074-133X
Vol 32 No. 6s (2025)

Comprehensive Numerical Analysis of Fluid Flow Characteristics in a Lid-Driven Cavity with a Central Obstacle: Flow Physics

Dalmalka Praveen Kumar[1*], Yadagiri Rameshwar[2]

E-mail: dalmalkapraveen@osmania.ac.in[1] , rameshwar@osmania.ac.in[2]

Affiliation

[1,2] Department of Mathematics, University College of Science, Osmania University, Hyderabad - 500007, India

Article History:

Received: *21-10-2024*

Revised: *05-12-2024*

Accepted: *12-12-2024*

Abstract:

Boundary layer flows and vortex dynamics are critical in understanding fluid motion in confined geometries. The lid-driven cavity (LDC) flow is a classical benchmark for analysing fluid behaviour under varying conditions, especially when obstacles are introduced. While past studies have explored primary and secondary vortex structures, the modulation of enstrophy and palinstrophy caused by obstacles has been underexplored. This study aims to bridge that gap by systematically investigating the effect of Reynolds numbers and obstacle aspect ratios on flow properties in a 2D LDC. To analyse the influence of Reynolds number (*Re*) and obstacle Aspect ratio (AR) on enstrophy (*Z*) and palinstrophy (*P*). To evaluate the enhancement in vortex dynamics and flow topology caused by introducing square obstacles at various aspect ratios within the cavity. To identify optimal configurations for improving fluid transport and mixing efficiency. An unsteady, laminar, incompressible flow of Newtonian fluid was simulated by the Finite volume-based Fractional Step Method. Square obstacles with aspect ratios AR=0L,0.4L, 0.5L, and 0.6L were placed at the centre of the cavity with numerical study for a range of *Re*=10,100,400, and 1000. The interaction between AR and *Re* dictates vortex dynamics in LDC flows. Higher AR disrupts flow symmetry through sharp-edge interactions, while increased *Re* elevates inertial effects, causing vortex splitting, secondary vortex formation, and improved fluid mixing. Obstacles boost *Z* and *P* by up to 53.08% and 50.85%, with the most significant increases for *AR* = 0.6L at *Re* = 1000 compared to a cavity without an obstacle. This suggests stronger vorticity gradients and enhanced mixing due to AR = 0.6L, as the obstacle occupies more of the cavity, restricting flow and creating stronger shear zones near the walls and the obstacle. At high *Re*, inertial forces dominate, leading to stronger vortex shedding, and more pronounced vorticity changes near sharp edges. Increasing *Re* from 10 to 1000 for AR = 0.6L raises *Z* and *P* by approximately 36.34% and 43.55%, illustrating a shift from viscous-dominated laminar to inertia-dominated flow, enhancing vortex strength, sharpening vorticity gradients, and improving mixing efficiency. The interplay between AR and *Re* dictates vortex dynamics, with higher AR disrupting symmetry and higher *Re* amplifying inertial effects, leading to vortex splitting, enhanced secondary vortices, and improved mixing. The increasing obstacle height amplifies *Z* and *P*, leading to improved fluid mixing and vortex dynamics, serving as effective tools for flow control and mixing enhancement in industrial and engineering applications.

Keywords: Lid-driven cavity, Rectangle obstacle, Vortices development, Enstrophy, Palinstrophy, Mixing enhancement.

1. Introduction

LDC problem with an obstacle has received considerable attention because of its vast applications in fluid dynamics; it has been investigated extensively and serves as a benchmark to test numerical methods and manifold code development [1,2]. Physics involved in LDC flow is relevant to vivid applications such as lake dynamics, heat exchangers, roll-coasting, galvanization, material processing, etc.[3,4].Burgraff [5] was the first to study the physical model of a 2D Lid-Driven Cavity (LDC) with block (obstacle), analysing the interactions between fluid flow and structure. He computed 2D LDCs to analyse velocity profiles, streamlines, and the analytical and numerical aspects of steady-separated flows. Pan and Acrivos [6] have investigated cavities of square and rectangular shapes with Creeping-flow streamline patterns, and cavities with finite and infinite depth. The authorized and accurate database is given by Ghia et al. [7] they reported comprehensive findings on the velocity fields along with the streamlines and vorticity contours for the different *Re* values ranging from 100 to 10000. Dhiman et al. [8] examined the way Reynolds number ($1 \le \mathrm{Re} \le 45$) and power-law index ($0.5 \le \mathrm{n} \le 2.0$) shape the steady cross-flow around an unconfined square cylinder and results indicate more extensive lateral disturbances for shear-thickening fluids, whereas shear-thinning fluids require finer grids to capture wake dynamics effectively. Hammami et al. [9] have studied the LDC in 3-D, and examined the unsteady nature of the flow in the cavity with and without an obstacle, they found that at critical value *Re*, the flow remains in a steady state for $Re < Re_{cri}$ and becomes unsteady for $\mathrm{Re} > Re_{cri}$. The results show that the essential value of Re without obstacle is greater than the critical value of *Re* with obstacle and the presence of an obstacle, the one-side LDC and two-sided LDC. Recently, two different papers authors, Huang et al. [10] and Rajan et al. [11] investigated 2-D conventional LDCs filled with various obstacles varying in sizes and shapes to clarify the effect of the size and position of the obstacle for different *Re* by using Lattice Boltzmann Method (LBM). Huang et al. (2020) [10] by LBM examined the internal 2-D circular obstacles with varying diameters below *Re* from 100 to 5000. When Renolds number *Re* increased, the secondary vortices near the obstacle became smaller, resulting in strong primary vortices. Based on the AR of an obstacle, when the obstacle increases, it gives rise to a bigger size of the secondary vortices near the top of it. To analyse the vortex, the shift in the cavity, the stream function and the positions of the primary and secondary vortices were evaluated against existing data. Rajan et al. [11], by the LBM, investigated LDCs with circular, elliptic and square shapes of obstacles placed in it, which led to exhibiting exceptional circulation regions and structures in comparison with classical LDC for *Re*=100, 400, and 1000 and obstacles position and size contribute to dramatic change in flow structure of fluid such as generated vortices, Splitting vortices and recirculation near the obstacles. The Streamlines, vorticity, and centerline velocity profiles are illustrated by them. Bisht et al. [12] used the LBM to explore the non-Newtonian fluids flow around obstacles in LDC. They found that variables like Reynolds number, obstacle size, and shape significantly impact the flow patterns and vortex formation. The study highlighted notable flow structure changes depending on the obstacles' size and configuration (Bisht et al. 2021). The lid-driven is a crucial benchmark for studying incompressible flows in confined volumes, focusing on flow evolution as the *Re* increases. This review covers topics from flow instabilities and numerical treatments to the transition to chaos in two-dimensional and three-dimensional flows and various extensions of the lid-driven cavity system Kuhlmann et al. [13]

(2018). Zhang et al. [14] (2022) conducted numerical work on LDC flow with embedded circular obstacles using spectral/hp element methods, focusing on different *Re* and obstacle diameters. The study visualized primary and induced vortices, capturing new vortex formations and demonstrating the efficiency and precision of the spectral/hp element methods. Requiring less preprocessing compared to the moving immersed boundary method and LBM. Bruneau & Saad [15] (2006), LDC problem discussed with global parameters such as enstrophy(*Z*), palinstrophy(*P*), and the qualitative essence of turbulent behaviour at high Reynolds numbers. We found the research gap focusing on less explored areas and findings to develop more comprehensive understanding of in vortex dynamics and flow topology for practical applications, Table 4 provides a clear, quantitative and followed by qualitative view of means by which increasing the Reynolds number along with aspect ratio of central squared obstacle enhances both enstrophy and palinstrophy as well flow dynamics (in Fig 4 and its description), with the changes reflecting the shift in flow behaviour from laminar to transitional and eventually more inertial-dominated flow which holds crucial insight into physics-involved flow dynamics in LDC with obstacles. We investigated the fundamental flow characteristics by analysing streamline (***ψ)*** patterns and vorticity (***ω***) contour distributions, with particular attention to sharp-edge interactions near walls of obstacles in observing variations in flow separation, vortex structures, and global characteristics, Renolds number (*Re*) together AR scaling effects, flow mixing mechanisms, and flow control parameters. Hence, we critically analyse the effects, as stated above, of the LDC flow problem with or without obstacles by changing the AR of rectangular obstacles as well as *Re* numbers 10,100,400 and 1000. we adopted the Fractional step method [16] on a staggered grid. The present work is organized into 4 sections. In continuation, Section 2 describes the problem and the numerical method used, fundamental equations with the boundary conditions of the LDC problem. by validating code and also in Table 1-3 In Section 3, the results and discussion, flow characteristics such as streamline and vorticity contour in Figures 3-4 and its assessment by subsections 3a,3b and 3c with the support of Tables 4-6. Finally, Section 4, outlines the principles and conclusions drawn.

2. Methods

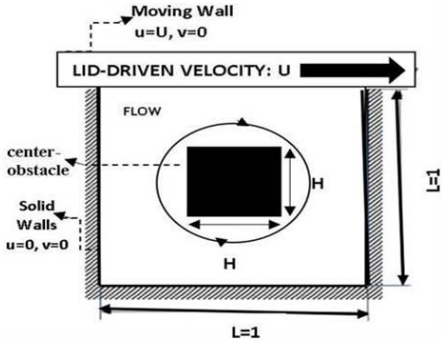

Figure 1. Schematic of LDC flow with internal square obstacle at the centre of a square cavity.

The governing equations in non-dimensional form are, the continuity equation (1) and momentum conservation equations (2) (as per Einstein's summation convection.) as follows: by eqn (3) to (7).

$$\frac{\partial u_i}{\partial x_i} = 0. \qquad (1)$$

$$\frac{\partial u_i}{\partial t} + \frac{\partial (u_j u_i)}{\partial x_j} = \frac{-\partial p}{\partial x_i} + \left(\frac{1}{Re}\right)\frac{\partial^2 u_i}{\partial x_j \partial x_j}. \quad (2)$$

Where u_i is velocity component, t is time, p is pressure, Re is Reynolds number and x_j are spatial coordinates for i, j which are spatial directions and summation is implied over repeated indices.

Initial conditions: t=0, 0≤ x ≤1, 0≤ y ≤ 1: u=0; v=0 (3)
Boundary conditions (BCs): t>0
Left wall
x =0, 0≤ y ≤1, u=0, v=0, (4)
Right wall:
x =L, 0≤ y ≤1, u=0, v=0, (5)
Bottom wall:
y =0, 0≤x≤1, u =0, v = 0, (6)
Top wall:
y =1, 0≤x≤1, u=1, v=0, (7)
The equations (1) and (2), are continuity and momentum equations resp., solved by Fractional step method.

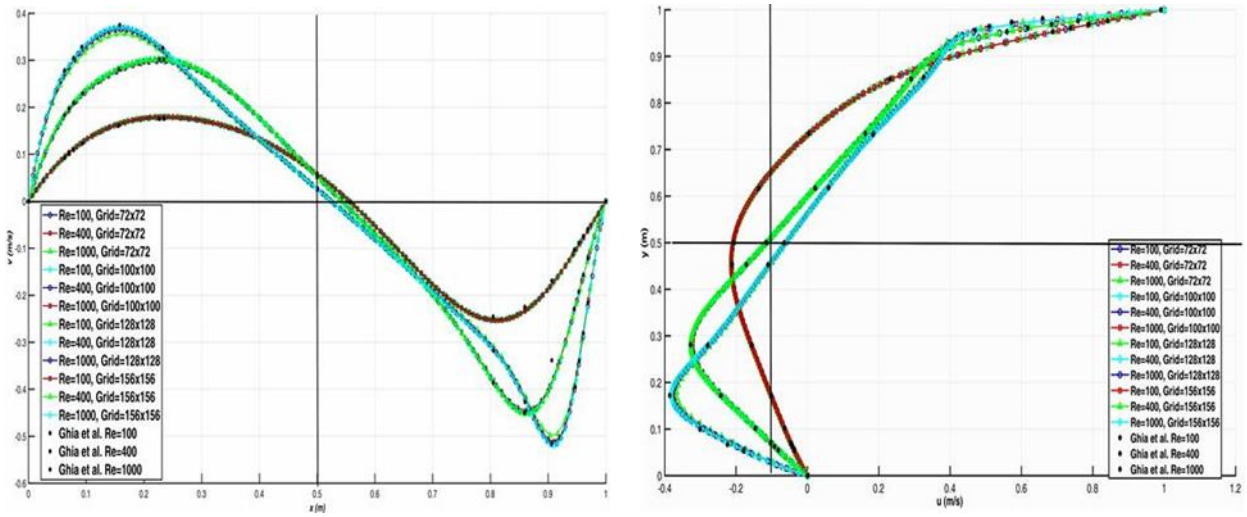

Figure 2. Vertical velocity along the x-axis. Horizontal velocity along the y-axis.

Table 1: Comparison of locations of vortex centers with [7] (at AR= 0.0, *Re* = 100, 400, and 1000).

***Re*, Validation, % error**	**Upper Right Vortex**		**Lower Left Vortex**		**Lower Right Vortex**	
	x	***y***	***x***	***y***	***x***	***y***
Present (*Re*=100)	0.61718750	0.74218750	0.031250	0.03906250	0.94531250	0.06250
Ghai *et al.* [7]	0.6172	0.7344	0.0313	0.0391	0.9453	0.0625
Deviation (%)	0	1.063	0	0	0	0
Present (*Re*=400)	0.55468750	0.60546875	0.05468750	0.0468750	0.8906250	0.1250
Ghai *et al.* [7]	0.5547	0.6055	0.0508	0.0469	0.8906	0.125
Deviation (%)	0	0	7.662	0	0	0

Present (*Re*=1000)	0.531250	0.57031250	0.08593750	0.0781250	0.86718750	0.11718750
Ghai *et al.* [7]	0.5313	0.5625	0.0859	0.0781	0.8594	0.1094
Deviation (%)	0	1.39	0	0	0.91	7.12

Note: Deviation (%) for coordinates x, y of some vortex centres are taken to be zero since Ghai et al. [7] gave only four decimal round-offs and the present work gave full decimal precision so for most of the present work's four decimal round-offs is exactly same.

Table 2: Comparison of positions maxima/minima *x*, *y* corresponding to centrelines *u*, *v* velocity components and its values corresponding values of ψ and ω with *Re* = 100, 400, and 1000 [7]

***Re*, Validation, % error**	***y(min)***	***u(min)***	***x (max)***	***v(max)***	***x(min)***	***v(min)***	***ψ (min)***	***ω***
***Re*=100 Present work**	0.453125	-0.210920	0.234375	0.175341	0.804688	-0.245431	-0.103389	-3.192007
Ghai *et al.* [7]	0.4531	-0.21090	0.2344	0.17527	0.8047	-0.24533	-0.103423	3.16646
Deviation (%)	0	0.009	0	0.041	0	0.041	0.033	0.81
***Re*=400 Present work**	0.281250	-0.3271469	0.2265625	0.3019410	0.8593750	-0.4497767	-0.113852	-2.292971
Ghai *et al.* [7]	0.2813	-0.32726	0.2266	0.30203	0.8594	-0.44993	-0.113909	2.29469
Deviation (%)	0	0.035	0	0.030	0	0.034	0.050	0.075
***Re*=1000 Present work**	0.1718750	-0.3814501	0.1562500	0.3693578	0.9062500	-0.5133620	-0.117422	-2.045723
Ghai *et al.* [7]	0.1719	-0.38289	0.1563	0.37095	0.9063	-0.51550	-0.117929	2.04968
Deviation (%)	0	0.376	0	0.429	0	0.415	0.430	0.193

Note: Values compared as Ghai et al. [7] with 128x128 grid for *Re* =100,1000, and 256 x256 grid for *Re* =400. Deviation (%) for minimum/maximum points of coordinates x, and y of the centreline velocity profile is taken to be zero since Ghai *et al.* [7] gave only four decimal round-offs and the present work gave full decimal precision to the present work four decimal round-offs are the same.

Table 3: Comparison of energy, enstrophy(*Z*) and palinstrophy(*P***)** with grid 128x128 for *Re* =1000 with **[**15]

Result	**Energy (*KE*)**	**Enstrophy(*Z*)**	**Palinstrophy(*P*)**
Present work	0.045635	18.405	0.15291 x 10^{+6}
Bruneau and Saad [15**]**	0.043721	17.685	0.15280 x 10^{+6}
Deviation (%)	3.55	4.07	0.072

3. RESULTS AND DISCUSSION

The code validation of the numerical method is tested without an obstacle for our simulation, and we have excellent agreement between our work and literature evident in Tables 1-3 and Table 5 shows the cores of primary, secondary vortices and even minimum/maximum points of the centreline velocity profile are very accurately agreed with Ghai et al. [7]. Both the graphs present the same trends: the non-dimensional centre line velocity, and streamline plot are validated for *Re*=100,400 and 1000. All the iterations are carried out up to many iterations where convergence criteria of 10^{-8} were met. The top lid was moving with a constant velocity of 1(m/sec). *Re* used in this computation are 10,100,400 and 1000. The non-denationalised velocity values with vertical, and horizontal lines via the cavity centre are shown in Figure 2 followed by streamline and vorticity contour plots in Figures 3 and 4, with their global flow characteristics. All three deviations of global parameters are well under 4.08%, which suggests relatively small differences between the present and reference values. $Z = \frac{1}{2}\iint_{\mathrm{A}} ||\omega||^2 d\mathrm{A}$, $P = \frac{1}{2}\iint_{\mathrm{A}} ||\nabla\omega||^2 d\mathrm{A}$, where $\omega = \frac{\partial v}{\partial x} - \frac{\partial u}{\partial y}$ is the vorticity denoting $\boldsymbol{V}_{\mathrm{ij}} = (u_{\mathrm{ij}}, v_{\mathrm{ij}})$ represents the velocity at the centre of a cell, for example kinetic energy $E = \frac{1}{2}\iint_{\mathrm{A}} ||\boldsymbol{V}||^2 \, d\mathrm{A}$, over domain *A* then *E* over the fluid region is $E_{fluid} = \frac{1}{2} \cdot$ (fluid cell area) $\cdot \sum\sum_{i,j}\left(u_{i,j}^2 + v_{i,j}^2\right)$, where each "fluid cell area" designates the area associated with a single fluid grid cell, and the summation spans all such cells within the fluid domain. For these *Z* and *P* are used in half of the work, validated against numerical results in Table 3 of Bruneau and Saad [15].

Streamline formations of the flow in enclosures with obstacles installed at the centre of the cavity are illustrated in Figure 3(d-l). In such cases, flow formation is not identical to the regular cavity without obstacles and with obstacles (compare Figure 3(a-d) and Figure 3(e-p)). These figures suggest that by increasing the *Re*, (column-wise images), a tiny vortex would develop on the bottom left and right corner of the bottom expand, as anticipated. Figure 3(a-d). Interestingly, the primary induced vortex grows as we increase *Re* and secondary vortices at both left- and right-hand sides reduce completely as we increase A.R. See Figure 3(e-p). The movement of the lid, which is uniform and is in the direction of the positive x-axis, generates a primary eddy (vortex) which encases the obstacle and hence holds a significant area in a cavity, leading to the induced eddy formed near the obstacle and the sharp corner obstacle improves the control and mixing flow characteristics. The top-right corner of the LDC and the leading edges of the rectangular obstruction are regions where local flow acceleration occurs due to flow compression, as per the principle of continuity. The recirculation area is positioned behind the obstacle, moving along the bottom of the cavity where the flow decelerates and reverses its direction. Thus, Figure 3 demonstrates the streamline pattern for *Re*=10,100,400,1000

employing the Fractional step method. In our work, we consider lower *Re* (*Re*=10,100,400) and a transitional *Re* (*Re* = 1000), along with the required AR, to effectively enhance mixing characteristics. In our earlier work (Kumar DP et al., [17]), we examined global parameters not only within the fluid domain but also across the entire domain including the obstacle region where velocity components are zero. This comprehensive investigation provided deeper physics insights —both quantitative and qualitative—into vortex development and fluid flow dynamics by varying the obstacle height *H* (while keeping its width *W* constant) in a LDCs with bottom-corner obstacles.

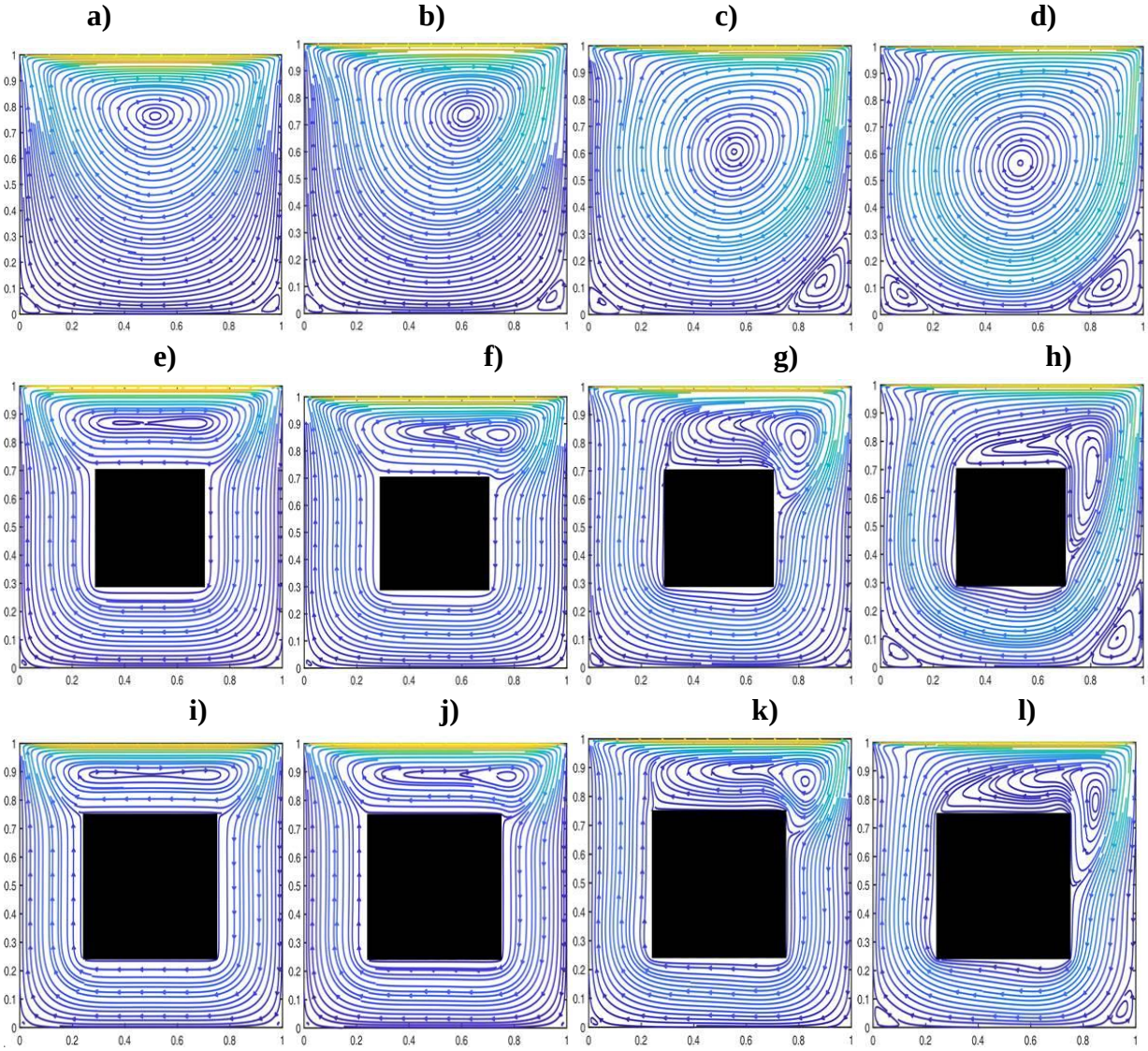

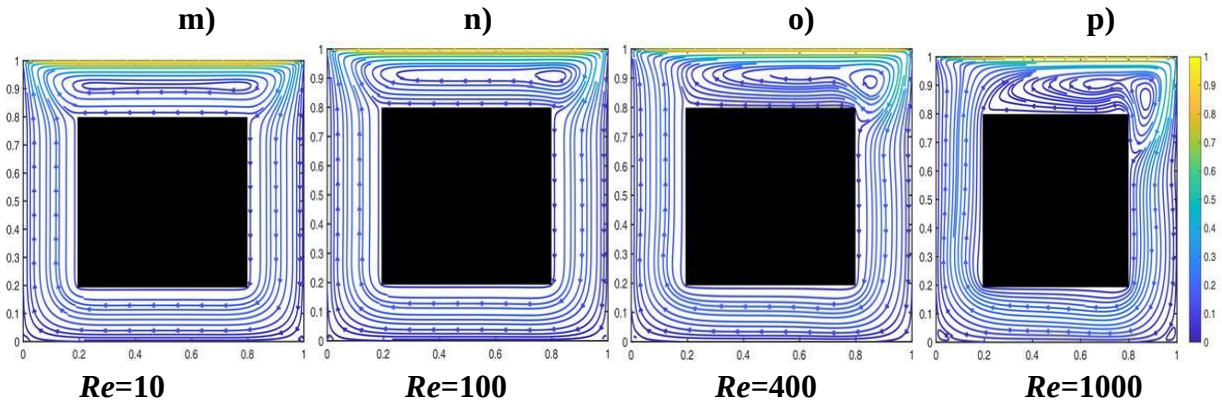

Figure 3. Variation of the streamlines with the aspect ratio in the first row is AR=0*L*, the Second is AR=0.4*L*, the third is AR=0.5*L*, and the fourth row is AR=0.6*L* with *Re*= 10, 100, 400 and 1000.

3a) Effect of Reynolds number and obstacle Aspect Ratio on fluid flow and vortex dynamics:

Obstacle's aspect ratio AR=0*L*:

In the case of *Re*=10,100,400 and 1000, AR=0, streamlines of LDC show us the primary vortex (larger circulation pattern in the middle) and secondary vortex (smaller circulation pattern in bottom corners) due to the geometrical shape of the square of a lid. In Figure 3(a-d), a common feature is flow, which is dominated by a large central vortex. For *Re*=10, Figure 3a, we observe that the induced primary vortex is positioned upwards, in the middle of the enclosure, and very small secondary eddies are induced at the bottom corners. Induced vortices formed due to the fluid flow are disrupted by a boundary or obstacle that causes the flow to separate or shear. As we increase *Re* to 100, we see the primary vortex shift to a bit right and the expansion of the secondary vortices. Further, with a rise in *Re* to 400, we see the primary vortex shifted to a bit down from the previous case position and much increased in size of the secondary vortices. Also, with a rise in *Re* to 1000, we see the primary vortex shifted a bit down, which is almost to the geometric centre of the cavity from the previous case position and much more enlarged in size of the secondary vortices due to the low viscosity related to *Re*=1000, which gives rise to increase in velocity and mobility of the fluid. Here, we observe that flow is characterised as laminar at low *Re* since viscous forces dominate over inertial forces. Moreover, vortices are small, stable and slowly evolving with no complex behaviour exhibition and an organised flow with smooth streamlines. This contrasts with higher *Re* and the prevalence of turbulent and more complicated patterns. In the view of a dynamical system, all cores are called centres, featuring clockwise rotation in a 2-D phase portrait by looking at steady-state flow solutions that look similar.

Obstacle's aspect ratio AR=0.4*L*:

In the case of Re=10, AR=0.4 from Figure 3e, the generated vortex is bifurcated, producing two sub-vortices, which have almost a vertical centrosymmetric with a right-side larger sub-vertex. Further, it is also interesting to note that both subvortices of the top are unified into one vortex with two centres on the left- and right-hand sides, and almost near the centre of them, a saddle point (x, y) = (0.483,0.869) exist. From Figure 3f and *Re*=100, a primary vortex has expanded to form a single induced vortex with one core on the hand side by the uniting of the two sub-vortices, and its saddle point has disappeared along with the vertex centre shifted in the direction of the lid motion.

Additionally, a tiny vortex can be observed in the left- and right-bottom enclosure's corners. From Figure 3h, in *Re*=400, the induced vortex, which is rotating clockwise in scoop-like form, becomes bigger and approaches close to the top right vicinity of the obstacle, and for *Re* greater than or equal to 400 as it grows, a lower corner vortex is induced which become increasingly visible. Finally, for *Re*=1000, due to the sharp slope of the rectangular obstacle, the bigger induced vortex moves downwards on the right side and will break down in parts by flow driven by the direction of lid movement. Also, a significant enhancement in the area of the bottom left- and right-hand side vortices is observed when compared to *Re*=10,100,400. As we observed in Figure 3(a-h) when compared to without obstacle (Figure 3d with Figure 3h), we see the primary/secondary vortices size drastically reduced due to the installation of obstacles at the geometric centre of the cavity.

Obstacle's aspect ratio AR=0.5*L*:

In the case of *Re*=10, AR=0.5 (Fig 3i), same as AR=0.5 but with reduced size of the generated vortex, which is bifurcated, producing two sub-vortices which have exactly a vertical centrosymmetric, both subvortices of the top are merged containing two cores on the left and right sides, next to the centre of them a saddle point (*x, y*) = (0.504,0.889) exist. In the case of *Re*=100, AR=0.5 (Figure 3j), we have a similar form, which becomes bigger but has a reduced vertex size due to pattern and flow field behaviour about saddle point disappearing as seen in Fig 3f the induced vortex, in scoop-like the bigger induced vortex moves downwards between the obstacle's right side and the cavity's right wall. Also, a new extra vortex (ternary vortex) is caused by the core at (*x,y*) =(0.678,0.231) at the bottom right side of the obstacle. We observed in Figures 3h and 3l that the secondary vortex size was reduced due to the increased aspect ratio of the obstacle.

Obstacle's aspect ratio AR=0.6*L*:

In the case of *Re*=10 with a new saddle point (x, y) = (0.512,0.909), also for *Re* =100 for AR=0.6 from Figure 3(j-l), the same pattern globally and behaviour of flow field but with further reduced induced vortex. Interestingly, in the cavity with the most significant obstacle (i.e., AR=0.6*L*) at *Re*=400, we notice that a single merge primary vortex in *Re*=100 as we increase *Re*=400, it gets split into two more induced vortices at the top near the centre and top right region of the rectangular obstacle. As we further increased *Re* to 1000, we observed in Figure 3p that the primary vortex ruptures and produced primary vortices on two sides of the obstacle. Thus leading to efficient control and improved mixing of fluid flow.

Table 4: Variation of Enstrophy (*Z*), Palinstrophy (*P*) with Reynolds Number (*Re*) and AR in LDC flow.

Re	**Aspect ratio (AR) (Height(*H*))**	**Enstro-phy (*Z*) of fluid region**	**% ↑ in *Z* for correspon d-ing *Re* from without obstacle**	**% ↑ in *Z* (from correspon d- ing *Re* to *Re*=1000)**	**Palinstro-phy (*P*) of fluid region**	**% ↑ in *P* for correspondin g *Re* from without obstacle**	**% ↑ in *P* (from correspon d ing *Re* to *Re*=1000)**
10	0.0*L*	11.679	-	122.59%	$4.1x10^{+04}$	-	119.51%

	0.40*L*	14.525	24.37%	57.78%	$4.8x10^{+04}$	17.07%	85.42%
	0.50*L*	17.135	46.71%	57.20%	$5.3x10^{+04}$	29.27%	78.00%
	0.60*L*	21.658	85.48%	36.34%	$6.2x10^{+04}$	51.22%	43.55%
100	0.0*L*	11.679	-	59.20%	$4.1x10^{+04}$	-	42.86%
	0.40*L*	14.928	27.83%	23.59%	$4.8x10^{+04}$	17.07%	43.55%
	0.50*L*	17.459	49.53%	24.69%	$5.4x10^{+04}$	29.27%	39.06%
	0.60*L*	21.906	87.57%	21.53%	$6.3x10^{+04}$	53.66%	18.67%
400	0.0*L*	14.840	-	26.40%	$4.7x10^{+04}$	-	18.42%
	0.40*L*	17.920	20.77%	9.90%	$5.5x10^{+04}$	17.02%	23.61%
	0.50*L*	20.188	36.06%	10.37%	$6.1x10^{+04}$	29.79%	21.92%
	0.60*L*	24.282	63.63%	8.61%	$7.1x10^{+04}$	51.06%	7.23%
1000	0.0*L*	19.286	-	-	$5.9x10^{+04}$	-	-
	0.40*L*	22.921	18.85%	-	$7.0x10^{+04}$	18.64%	-
	0.50*L*	25.465	32.01%	-	$7.7x10^{+04}$	30.51%	-
	0.60*L*	29.528	53.08%	-	$8.9x10^{+04}$	50.85%	-

Note: The table summarizes the enstrophy (*Z*) and palinstrophy (*P*) values for different Reynolds numbers (*Re*) and obstacle aspect ratio (*AR*), alongside percentage increases relative to reference cases (without obstacle and *Re*=1000). Symbols '-' are not required as they are zero since they represent percentages on the same values.

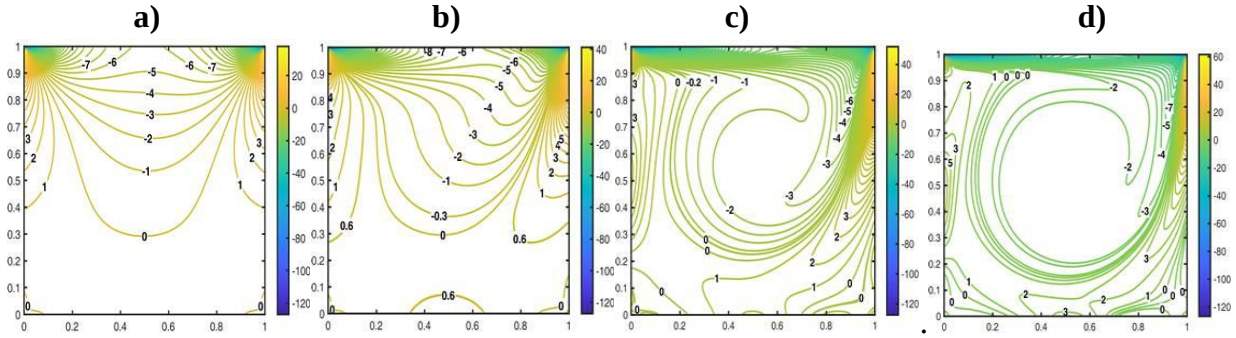

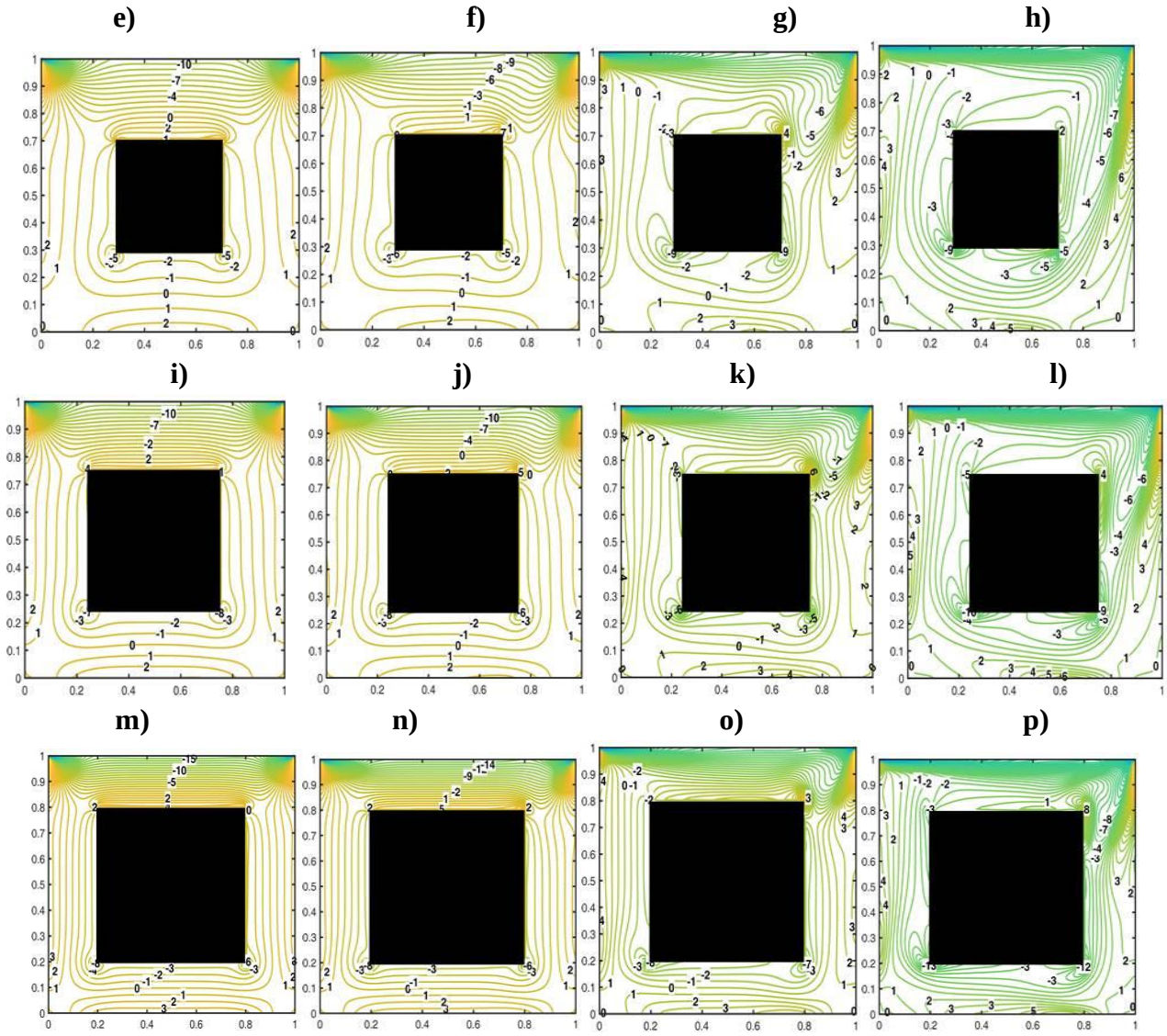

Figure 4. Vorticity contour plots show variations with different aspect ratios: the first row displays AR=0*L* (no obstacle), the second row AR=0.4*L*, the third row AR=0.5*L*, and the fourth row AR=0.6*L*. Each column presents results at Reynolds numbers *Re* of 10, 100, 400, and 1000.

3b) Effect of Reynolds number and obstacle Aspect Ratio on enstrophy and palinstrophy in LDC:

The vorticity contour plots in the provided Figure 4 and Table 4 provide key insights into the dynamics of enstrophy (*Z*) and palinstrophy (*P*) in LDC flows are governed by the complex interplay of Reynolds number (*Re*) and obstacle height (aspect ratio, AR), which influence the flow structure, energy redistribution, and mixing intensity. This study demonstrates variations in AR and *Re* affect vortex formation, energy cascades, and mixing efficiency through detailed analysis of the flow fields, with a particular focus on *Z* (a measure of vorticity intensity) and *P* (a metric for vorticity gradient magnitudes). In the absence of obstacles (AR=0.0*L*), the cavity flow exhibits a dominant primary vortex whose structure is dictated primarily by the balance of viscous and inertial forces. At low *Re* =10, viscous effects dominate, leading to weak rotational structures and minimal *Z* with 11.679) and

P with 4.1x10^{+04}) values. As *Re* increases, inertial effects amplify vorticity production and induce secondary vortex formation near the cavity corners. This results in higher *Z* and *P* values, with sharp gradients appearing at the boundaries of the primary vortex, which reflects the redistribution of energy into smaller flow structures. For *Re*=1000, the flow becomes increasingly dominated by inertial forces, resulting in stronger vortex interactions, enhanced mixing, and significant increases in both *Z* (with 19.286) and *P* (with 5.9x10^{+04}) values.

The introduction of obstacles modifies the flow by disrupting the primary vortex, enhancing secondary vortex formation and even tertiary vortex if present. For intermediate obstacle aspect ratios (AR=0.4*L*,0.5*L*), the sharp edges of the obstacle act as the positions for vorticity production due to flow separation and recirculation zones which are evident as shown in Figure 4e-4l. At *Re* = 10, the obstacle induces minor increases in *Z* by 24.37% and 46.71%, and in *P* by 17.07% and 29.27% for AR = 0.4*L* and 0.5*L*, respectively, compared to the reference case without the obstacle, as the flow remains largely governed by viscous effects. However, at *Re*=100 and *Re*=400, inertial forces drive significant vortex stretching, splitting and interactions with the obstacle's sharp edges particularly near top right the sharp edge of the obstacle and stagnatin points on top left and right corners of cavity, which amplify the energy in the flow's rotational structures and enhance *Z* and *P* as shown in values of Figure 4. At *Re*=1000, the interaction between the primary vortex and the obstacle sharpens vorticity gradients, producing stronger secondary vortices associated with higher inertial forces in the flow and leading to the third-largest peak in both *Z* with 22.92 and *P* with 7.0x10^{+04} values. The highest obstacle height (AR=0.6*L*) demonstrates the most pronounced effects across all *Re*. The larger obstacle increases flow separation and promotes the formation of smaller, high-energy vortices, which are indicative of an enhanced cascade of energy to smaller scales. At low *Re*, the obstacle moderately increases *Z* (21.66%) and *P* (51.22%) compared to the reference case without the obstacle, reflecting stronger vortex structures even in laminar regimes. At *Re*=100 and *Re*=400, the obstacle generates higher vorticity gradients due to enhanced interactions between the primary and secondary vortices especially near obstacle sharp edges where the flow undergoes abrupt directional changes. This will lead even more to higher *Re* which is evidenced by sharper velocity profiles, sharp changes in vorticity across the fluid domain and increased *Z* and *P* values. Thus, for *Re*=1000, the obstacle produces intense vortex breakdown and turbulent mixing, maximizing *Z* (53.08% increase) and *P* (50.85% increase), due to the concentrated shear layers near the obstacle and the enhanced energy transfer to smaller scales. Larger central obstacles in LDC flows fundamentally alter the flow dynamics by intensifying vortex generation and interactions, leading to multiple vortical structures. Thus, in essence, the increased obstacle height enhances enstrophy levels through stronger velocity gradients and vorticity production. This results in a more complex flow topology with modified shear layer behaviour and distinct high-vorticity regions, as evidenced in both streamline and vorticity contour plots. Even higher Reynolds numbers drive the dominance of inertial forces over viscous effects, promoting vortex stretching and rotation, especially when obstacles induce flow separation and shear-layer instability that generate steep vorticity gradients.

Table 5. Position of generated primary vortex and secondary vortex centres for LDC installed rectangular obstacles**.**

(*Re*)	Vortex produced by the obstacle					Left secondary vortex		Right secondary vortex	
	Aspect ratio	Left vortex above the obstacle		Right vortex above the obstacle		*x*	*y*	*x*	*y*
		x	*y*	*x*	*y*				
10	**AR=0**	**Primary Vortex (without obstacle)**				0.0391	0.0391	0.9609	0.0391
		x 0.5156		*y* 0.7656					
	AR=0.4	***x***	***y***	***x***	***y***	0.0234	0.0156	0.9844	0.0234
		0.3906	0.8672	0.6563	0.8672				
	AR=0.5	0.3203	0.8906	0.7109	0.8906	0.0156	0.0156	0.9844	0.0156
	AR=0.6	0.2578	0.9141	0.7656	0.9141	0.0156	0.0156	0.9922	0.0156
100	**AR=0**	**Primary Vortex (no obstacle)**				0.0391	0.0313	0.9453	0.0625
		x 0.6172		*y* 0.7422					
	AR=0.4	***x***	***y***	***x***	***y***	0.0156	0.0234	0.9844	0.0234
		-	-	0.7421	0.8594				
	AR=0.5	-	-	0.7813	0.8828	0.0156	0.0156	0.9844	0.0156
	AR=0.6	-	-	0.8125	0.9063	0.0156	0.0156	0.9922	0.0156
400	**AR=0**	**Primary Vortex (no obstacle)**				0.0547	0.0469	0.8906	0.125
		x 0.55469		*y* 0.60936					
	AR=0.4	***x***	***y***	***x***	***y***	0.0313	0.0313	0.9688	0.0313
		-	-	0.7969	0.8125				
	AR=0.5	-	-	0.8281	0.8516	0.0234	0.0234	0.9844	0.0234
	AR=0.6	-	-	0.8516	0.8281	0.0234	0.0234	0.9844	0.0234
1000	**AR=0**	**Primary Vortex (no obstacle)**				0.0859	0.0781	0.8672	0.1172
		x 0.53125		*y* 0.57031					
	AR=0.4	***x***	***y***	***x***	***y***	0.0703	0.0547	0.9063	0.1094
		-	-	0.8047	0.6875, and 0.7109				
	AR=0.5	-	-	0.8516	0.7969	0.0469	0.0391	0.9531	0.0625
	AR=0.6	0.6519	0.9063	0.8750	0.8516	0.0313	0.0234	0.9766	0.0313

Note: x and y (not bold letter) coordinates of the centre of the primary vortex and ***x*** and ***y*** (***x, y*** bold letters) coordinates of the centre of the secondary vortex's left and right vertices in Table 5, whereas in Table 6, ***x*** and ***y*** **(bold letters)** coordinates of stagnation point on obstacles. Dash indicates (-) in Table 5, no primary or secondary vortices cores, whereas Table 6 indicates no stagnation points observed.

Table 6. Position of Stagnation points on the right side of the obstacle and max. and min. of *p, u, v* values.

Reynolds number (*Re*)	**Aspect Ratio (AR)**	**Stagnation points**		**Pressure distribution**		**Velocity distribution**			
		x	***y***	**Max.(*p*)**	**Min.(*p*)**	**Max.(*u*) and Max.(*v*)**		**Min.(*u*) and Min.(*v*)**	
						u	*v*	*u*	*v*
10	AR=0	-	-	19.384	-18.606	1	0.3694	-0.2081	-0.3986
	AR=0.4	0.703	0.703	20.20	-19.64	1	0.3668	-0.1874	-0.3852
	AR=0.5	0.75	0.745	20.84	-20.39	1	0.3655	-0.1875	-0.3802
	AR=0.6	0.797	0.793	22.08	-21.82	1	0.3622	-0.1886	-0.3752
100	AR=0	-	-	2.4351	-1.6040	1	0.3132	-0.2429	-0.5330
	AR=0.4	0.703	0.6838	2.4101	-1.7272	1	0.3139	-0.2080	-0.4748
	AR=0.5	0.75	0.7374	2.4398	-1.8090	1	0.3143	-0.2059	-0.4590
	AR=0.6	0.797	0.7855	2.5256	-1.9641	1	0.3150	-0.2033	-0.4383
400	AR=0	-	-	1.0696	-0.2916	1	0.3199	-0.3365	-0.6364
	AR=0.4	0.703	0.581	1.0012	-0.3361	1	0.2403	-0.2317	-0.6154
	AR=0.5	0.75	0.667	0.9809	-0.3557	1	0.2398	-0.2128	-0.5990
	AR=0.6	0.797	0.745	0.9658	-0.3833	1	0.2395	-0.2192	-0.5753
1000	AR=0	-	-	0.7460	-0.0727	1	0.3772	-0.3841	-0.6591
	AR=0.4	0.703	0.394	0.6903	-0.0949	1	0.2811	-0.2916	-0.6613
	AR=0.5	0.75	0.491	0.6689	-0.1067	1	0.2523	-0.2620	-0.6586
	AR=0.6	0.797	0.643	0.6470	-0.1234	1	0.2430	-0.2418	-0.6491

3c) Velocity distribution:

The analysis of velocity distribution in a lid-driven cavity (LDC) flow with embedded obstacles highlights critical flow dynamics shaped by varying aspect ratios (AR) and Reynolds numbers (*Re*) see (Table 6). The maximum horizontal velocity (max(*u*)) remains consistently at 1 across all configurations, indicating a strong influence on the top wall's motion. At *Re* = 100, min(*u*) increases by approximately 16.3% from AR = 0 to AR = 0.6, indicating a reduction in reverse flow intensity. Similarly, at *Re* = 400, min(*u*) increases by about 34.8% from AR = 0 to AR = 0.6, showing greater flow stabilization with increasing AR. At *Re* = 400, min(*v*) decreases by approximately 9.6% from AR = 0 to AR = 0.6, underscoring substantial fluctuations in downward flow. However, the minimum horizontal velocity (min(*u*)) varies with a mean of approximately -0.234 and a standard deviation of 0.031, reflecting moderate variability as AR and *Re* change. This variability suggests that the reverse flow's intensity is significantly influenced by the cavity's geometric constraints and flow parameters. And enhancing the induced vortex to manage the system’s process parameters and mixing In contrast, the vertical velocity component (*v*) exhibits greater sensitivity. The mean maximum vertical velocity (max(*v*)) is about 0.320, with a standard deviation of 0.045, indicating a relatively stable upward flow across different conditions. However, the minimum vertical velocity (min(*v*)) presents a broader

spread, with a mean of -0.541 and a higher standard deviation of 0.085, indicating significant fluctuations in the downward flow. These statistical insights suggest that while the horizontal flow is more consistent, the vertical flow is more susceptible to changes in AR and *Re*, leading to substantial variations in the overall flow dynamics, which are important for optimizing fluid behaviour.

4. Discussion

Numerical results show that the Fractional step method which is more efficient can accurately simulate the LDC problem. This study presented in the paper reveals that the phenomenon of fluid flow is linked to varying the Renolds number (*Re)*, and obstacle Aspect ratio (AR) where increasing *Re* and *AR* significantly enhances both enstrophy (*Z)* and Palinstrophy *(P)*, with larger obstacles and high inertial effects contributing to pronounced vortex dynamics, energy redistribution, and mixing efficiency. Understanding the flow behaviours change with varying AR and *Re* is critical for optimizing designs in engineering applications, including turbulent mixing, energy-efficient fluid systems, and flow control technologies. This work addresses a significant gap by quantifying the effects of obstacles on both large-scale vorticity intensity (*Z*) and fine-scale flow gradient sensitivity (*P*), offering insights applicable across industrial and scientific domains.

The following are key insights of the work:

1) At higher *Re*, inertial forces dominate, vortices interact more strongly and mixing is enhanced as reflected in sharp increases in enstrophy (*Z*) which is a measure of vorticity intensity with increasing *Re* (as in Table 4) from 11.679 at *Re*=10 to 19.286 at *Re*=1000 for without obstacle (AR=0) marking a 122.59% increase, showing a strong correlation between *Re* and vorticity intensity. The slower growth at higher *Re* (26.40% for *Re*=400 to 1000) reflects saturation of vorticity production which is true in all AR as shown in Table 4.

2) In the impact of obstacle aspect ratio (AR) view, obstacle presence amplifies *Z* by enhancing vortex generation, with moderate ARs (0.4*L* and 0.5*L*) obstacles displaying nearly identical trends. Their increases (57.78% and 57.20% for *Re*=10 to 1000) suggest similar effects on flow separation and recirculation zones, despite slight divergence at mid-*Re* values (0.5L exhibits a higher 24.69% increase for *Re*=100 to 1000). For AR = 0.6*L*, despite having the smallest overall growth (36.34%), larger obstacles significantly disrupt flow symmetry and induce more pronounced vortex breakdown, causing *Z* to increase in unique ways. The smaller percentage increases at higher *Re* (8.61% for *Re*=400 to 1000) reflect energy redistribution into finer-scale turbulence. In the vortex dynamics view, the complexity of the flow, reflected in the enstrophy levels, intensifies with larger obstacles and higher *Re* owing to pronounced shear layers and enhanced rotational energy.

3) In the gradient magnitude sensitivity aspect Palinstrophy (*P*), representing vorticity gradient magnitudes, increases sharply with *Re*, reflecting higher energy concentration in flow structures evident from AR=0.0*L*, without obstacles, *P* increases sharply (119.51%) from *Re*=10 to *Re*=1000, showing uninhibited energy transfer into concentrated vortices. The sharp decline at higher *Re* (18.42% for *Re*=400 to 1000) mirrors diminishing shear-layer gradients.

The role of obstacles in intermediate obstacles ARs (0.4*L* and 0.5*L*), at AR = 0.4*L* **e**xhibits the largest growth overall (85.42%) and remains more sensitive at intermediate *Re* (23.61% for *Re*=400 to 1000). This suggests that moderate obstacles optimize the formation of high-gradient flow zones. AR=0.5*L* follows similar trends to AR=0.4*L* with slightly reduced values, achieving 78.00% growth for *Re*=10

to1000 and 21.92% for *Re*=400 to1000. The slightly lower *P* increase may reflect subtler flow separation effects compared to 0.4*L*.

4) The largest obstacles AR=0.6*L*, exhibit the lowest overall growth (43.55%), consistent with diminishing gradient intensities in flows disrupted by significant vortex breakdown. The low growth at higher *Re* (7.23% for *Re*=400 to 1000) indicates energy is increasingly distributed across broader scales rather than concentrated in small vortices. Enhanced energy cascades, shear-layer instabilities, and increased velocity gradients near obstacles all contribute to higher *P* ($8.9 \times 10^{+04}$) value, particularly at higher *Re.*

5) We investigate the influence of aspect ratio (AR) and Reynolds number (*Re*) on a centred obstacle, with AR varying from 0*L* to 0.6*L*. As *Re* increases (from *Re*=10 to *Re*=1000), the size of the generated primary vortex grows significantly, accompanied by increases in velocity magnitude and vorticity above the obstacle. Notably, for non-zero AR configurations by increasing AR, the secondary vortices in the bottom-right and left corner are significantly diminished or completely vanish compared to the case without an obstacle (AR=0), as illustrated in Figure 3(a–c). Additionally, stagnation points were observed both on the obstacle's surface and along the domain boundaries, reflecting the intricate flow dynamics induced by the obstacle's presence evident in Figure 3 and corresponding Table 6 for it.

6) The aspect ratio (AR) and Reynolds number (*Re*) have a core impact on pressure (*p*) distribution. At lower *Re* (for *Re*=10), increasing AR significantly enhances maximum pressure (max(*p*)), whereas, at higher *Re* (for *Re*=1000), the influence of AR on max(*p*) diminishes, leading to a more complex interplay between fluid mixing and pressure gradients as in Table 6.

7) Low and intermediate Reynolds numbers (*Re*) are selected to enhance mixing due to the large vortex generated as the aspect ratio (AR) of the obstacle increases. This results in a more compact flow region and increased velocity to maintain continuity. The primary vortex moves clockwise, while the secondary and tertiary vortices move counterclockwise, even with an obstruction. Localized velocity fluctuations occur near the leading edges of the obstruction, but overall flow characteristics remain consistent with the turbulent regime. At intermediate Reynolds numbers (*Re* = 400 to 1000), flow separation behind the obstacle becomes more pronounced, and evident of vortex shedding or the formation of wake regions.

8) Pressure changes are most pronounced near the obstruction, particularly at the leading edges, where flow separation and localized acceleration cause pressure dips. While Bernoulli's principle can partially explain these dips along specific streamlines, the overall pressure field is influenced by complex vortex dynamics and viscous effects. The rest of the cavity generally exhibits a more uniform pressure distribution, resembling an unobstructed scenario. However, the obstruction induces flow restrictions and creates low-pressure zones that alter the flow structure and pressure gradients throughout the cavity, especially at higher Reynolds numbers.

5. Acknowledgments:

The authors express their profound gratitude to the Indian Institute of Technology Bhubaneswar (IIT Bhubaneswar) for their invaluable support and for providing access to the high-performance Computational Lab for an extended one-month duration, which was instrumental in conducting this research. Special thanks are extended to Dr. Yogesh G. Bhumkar, Associate Professor, School of

Mechanical Sciences, for his unwavering encouragement, insightful guidance, and commitment to fostering excellence in research. His mentorship played a pivotal role in achieving meaningful outcomes.

6. Conflict of interest:

Authors have no conflict of interest

References:

[1] Kuhlmann, Hendrik. (2018). *The Lid-Driven Cavity. Cham:* Springer Nature Switzerland. doi:10.1007/978-3-319-91494-7_8.

[2] Shankar, P. N., & Deshpande, M. D. (2000). *Fluid mechanics in the driven cavity*. Annual Review of Fluid Mechanics, 32, 93–136. doi: 10.1146/annurev.fluid.32.1.93.

[3] Chhabra, R. P., & Richardson, J. F. (1999). *Non-Newtonian flow and rheology in turbulent processes.* Oxford: Butterworth-Heinemann.

[4] Nakamura, M., & Sawada, T. (1988). *Numerical study on the flow of a non-Newtonian fluid through an axisymmetric stenosis.* ASME Journal of Biomechanical Engineering, 110(2), 137–143. doi:10.1115/1.3168588.

[5] Burggraf, O. R. (1966). *Analytical and numerical studies of the structure of steady separated flows.* Journal of Fluid Mechanics, 24(1), 113–151. doi:10.1017/S002211206600046X.

[6] Pan, F., & Acrivos, A. (1967). *Steady flows in rectangular cavities.* Journal of Fluid Mechanics, 28(4), 643–665. doi:10.1017/S0022112067001663.

[7] Ghia, U., Ghia, K. N., & Shin, C. T. (1982). *High-Re solutions for incompressible flow using the Navier-Stokes equations and a multigrid method*. Journal of Computational Physics, 48(3), 387–411. doi:10.1016/0021-9991(82)90058-4.

[8] Dhiman, A. K., Chhabra, R. P., & Eswaran, V. (2006). *Steady Flow of Power-law Fluids Across a Square Cylinder.* Chemical Engineering Research and Design, 84(4), 300–310. doi:10.1205/cherd05017

[9] Hammami, F., Ghorbel, A., & Cheikh, N. B. (2017). *Computational analysis of fluid flow due to a two-sided lid driven cavity with a circular cylinder.* International Journal of Computational Fluid Dynamics, 31(7), 317–328. doi:10.1080/10618562.2017.1330795.

[10] Huang, T., Yang, B., & Chen, F. (2020). *Simulation of Lid-Driven Cavity Flow with Internal Circular Obstacles.* Applied Sciences, 10(19), 6675. doi:10.3390/app10196675.

[11] Rajan, I., & Perumal, D. (2021). *Flow dynamics of lid-driven cavities with obstacles of various shapes and configurations using the Lattice Boltzmann method.* Journal of Thermal Engineering, 83-102. https://doi.org/10.18186/THERMAL.869135.

[12] Bisht, M., Kumar, P., & Patil, D. (2021). *Non-Newtonian power-law fluid flow over obstacles embedded inside a cavity.* Physics of Fluids, 33, 043111. https://doi.org/10.1063/5.0046655.

[13] Kuhlmann, H., & Romanò, F. (2018). *The Lid-Driven Cavity.* Computational Methods in Applied Sciences. https://doi.org/10.1007/978-3-319-91494-7_8.

[14] Zhang, J., Xiao, B., & Yang, W. (2022). *Numerical Study of Lid-Driven Square Cavity Flow with Embedded Circular Obstacles Using Spectral/hp Element Methods*. Applied Sciences. https://doi.org/10.3390/app122211711.

[15] Bruneau, C., & Saad, M. (2006). *The 2D lid-driven cavity problem revisited*. Computers & Fluids, 35, 326-348. https://doi.org/10.1016/J.COMPFLUID.2004.12.004.

[16] Kim, J., & Moin, P. (1985). *Application of a fractional step method to incompressible Navier Stokes equations.* Journal of Computational Physics, 59(2), 308–323. doi:10.1016/0021-9991(85)90148-2.

[17] Kumar DP, Rameshwar Y, Ali R, Nazari S, Kallel M, Galal AM. *Computational analysis of Newtonian fluid in a 2-D square cavity with kinetic energy, enstrophy, and palinstrophy in the presence of bottom corner obstacle*. Results Phys. 2024;108086. https://doi.org/10.1016/j.rinp.2024.108086